Characterization of spatially curved beams with anisotropically adaptive stiffness using sliding torsional stiffeners

Nobaveh, Ali Amoozandeh; Radaelli, Giuseppe; van de Sande, Werner W.P.J.; van Ostayen, Ron A.J.; Herder, Just L.

DOI
10.1016/j.ijmecsci.2022.107687

Publication date
2022

Document Version
Final published version

Published in
International Journal of Mechanical Sciences

Citation (APA)
Nobaveh, A. A., Radaelli, G., van de Sande, W. W. P. J., van Ostayen, R. A. J., & Herder, J. L. (2022). Characterization of spatially curved beams with anisotropically adaptive stiffness using sliding torsional stiffeners. *International Journal of Mechanical Sciences*, *234*, Article 107687. https://doi.org/10.1016/j.ijmecsci.2022.107687

International Journal of Mechanical Sciences 234 (2022) 107687

Contents lists available at ScienceDirect

International Journal of Mechanical Sciences

journal homepage: www.elsevier.com/locate/ijmecsci

Characterization of spatially curved beams with anisotropically adaptive stiffness using sliding torsional stiffeners

Ali Amoozandeh Nobaveh *, Giuseppe Radaelli, Werner W.P.J. van de Sande, Ron A.J. van Ostayen, Just L. Herder

Precision and Microsystems Engineering Department, Delft University of Technology, 2628CD, Delft, The Netherlands

ARTICLE INFO

Keywords:
Spatially curved beams
Anisotropically variable stiffness
Torsional stiffening
Complaint mechanism

ABSTRACT

Compliant mechanisms (CM) with adaptive stiffness have been widely used in robotics and machine design applications. This paper proposes adapting the endpoint stiffness of a spatially curved compliant beam using a movable torsional stiffener and a new graphical characterization method for the resulting anisotropic stiffness of the endpoint for large deflections. A slender clamped-free cruciform beam with a predetermined spatial shape was utilized as the main compliant part, and a shorter sliding bellow was served as the torsional stiffener. The beam's endpoint displacements are mainly determined by its bending and torsional deformations. Therefore, the relocation of a bellow stiffener with high torsion and low bending stiffness along the described beam with relatively low torsion and high bending stiffness led to notable changes in the kinetostatic behavior at the endpoint. The share of bending and torsional stiffness of elements along the beam to endpoint stiffness varies depending on the direction. Experiments with arbitrarily chosen parameters of the current design reveal an anisotropically adaptive stiffness with 21.5 times more stiffness variations in one direction compared to the other. Effective characteristics for this behavior, such as the length and position of the bellow, were explored in an effort to improve it. To capture the effect of these parameters, the Isoforce Displacement Closed Surface (IDCS) was introduced as a new characterization method to visualize the nonlinear kinetostatic behavior of a CM throughout its three-dimensional range of motion. The IDCS was further used to elucidate how individual components of the current mechanism contribute to the system's overall kinetostatic behavior. Experiments were done on prototypes to confirm the changes in endpoint stiffness that were predicted by simulations.

1. Introduction

Variable stiffness is a topic of interest in a wide variety of research fields. There are numerous examples in aerospace engineering, soft robotics, medical devices, smart materials, and wearable robotics. Despite the fact that these applications are different, the shared desired characteristic is that the designed devices must be able to alter their stiffness in a specified direction on demand.

In aerospace engineering, variable stiffness structures can be found in shape morphing applications [1–4]. Through shape morphing, wings can change their shape to become more efficient across various flight conditions. Kuder et al. [5] reviewed concepts for variable stiffness with a focus on shape morphing for aerospace applications, and Sun et al. [6] reviewed the same concept based on smart materials and structures.

Variable stiffness solutions were also explored in the field of soft robotics. Manti et al. [7] reviewed concepts for variable stiffness for application in this field. In soft robotics, the focus is mainly on using variable stiffness parts for the different phases of the interaction of soft robots with natural environments [8–10]. There are a handful of examples in soft robotics grippers which change the stiffness during different phases of grasping and handling the material using different techniques such as granular jamming, which can be defined as transition of granular media from fluid like to solid like state [11–13]. or layer jamming [14–16] and hybrid jamming which includes a combination of both techniques [17]

In medical applications, variable stiffness is a topic of interest mainly in surgical equipment where the stiff mode is used for cutting, grasping, or supporting other equipment while the soft mode is needed for traveling inside the body [18–20]. Blanc et al. [21] reviewed variable stiffness mechanisms for the application of medical devices.

In smart materials, taking advantage of variable stiffness can be the functionality basis of several proposed designs, where the effect of temperature or input voltage causes different stiffness characteristics of the structure [22,23].

* Corresponding author.
E-mail address: a.amoozandehnobaveh@tudelft.nl (A.A. Nobaveh).

https://doi.org/10.1016/j.ijmecsci.2022.107687
Received 15 March 2022; Received in revised form 2 August 2022; Accepted 21 August 2022
Available online 30 August 2022

Adjusting stiffness can also be used in wearable robotics, where changing the stiffness of slender and lightweight structures is demanded to support different phases of human motion, e.g., different states of the upper body or limbs in their range of motion [24–26].

Numerous techniques for altering the stiffness of a system and characterizing these variations have been developed for a variety of applications. [27–30]. However, the majority of these techniques are designed in a complex and obtrusive manner. Still, in some applications, e.g., aerospace or wearable robotics, slenderness and being lightweight are key requirements. For instance, morphing aircraft wings using traditional mechanical actuators and mechanisms is often not viable due to the additional weight of these mechanisms [31,32]. Similarly, the weight of wearable robots should be kept as low as possible to minimize the load that the user must bear [33–35]. On the other hand, these applications mostly need to perform relatively complex motion or support in three-dimensional space, which would commonly result in a complex assembly of several parts [36,37]. However, adding complexities can wipe out the core functionality of the mechanism for these specific applications.

A spatial Compliant Mechanism (CM) could be used to address these types of intricate requirements for a relatively simple and slender system [38–41]. These mechanisms gain their motion as well as support the force from the elastic deformation of spatially curved parts [42,43]. This type of CMs is still underexplored. A notable example of this type of topology is a clamped-free slender beam, in which the elements of the curved beam affect endpoint behavior [44], similar to an open chain robotic arm, in which the entire system contributes to end-effector behavior. Here, mainly the bending and torsional stiffness of elements along the beam contribute to the endpoint kinetostatic behavior. Hence, it is possible to use these parameters to adapt the endpoint stiffness. There are several examples in the literature, mainly focusing on changing the local bending stiffness of elements to adapt the overall stiffness of the system. Methods like layer coupling have been widely used [45–47], in these examples, a mechanism locally decouples layers to reduce the bending stiffness of the endpoint.

The majority of research cited thus far has focused exclusively on adapting a system's bending stiffness in order to design a planar mechanism. In spatial mechanisms, the endpoint behavior is not only dependent on the bending stiffness of elements along the shape but also strongly influenced by the torsional stiffness of these elements [48]. There is no doubt that by utilizing torsion as a primary stiffness tailoring tool in spatial mechanisms, higher and more sophisticated stiffness change ratios are achievable. However, implementing torsional stiffness changes has received little attention [49,50].

In this article, adapting the endpoint stiffness of a spatially curved compliant clamped-free beam using a sliding torsional stiffener is investigated, and a new graphical characterization is proposed for the characterization of the resulting anisotropic stiffness of the endpoint for large deflections. It is shown that the endpoint secant stiffness under large deflections can notably change when the stiffener length and position on the beam alter. Two key compliant parts with contrasting mechanical behavior were used: a bellow as a torsional stiffener and a spatially curved prismatic beam with a cruciform cross-section as the base part. It is shown that the changes in the beam's endpoint stiffness are highly anisotropic. These changes in endpoint kinetostatic behavior were determined by different bellow configurations and then captured by the definition of a graphical characterization method, Isoforce Displacement Closed Surface (IDCS), and a metric, Displacement Change (DC). The IDCS was defined to visualize the nonlinear spatial kinetostatic behavior of the CM for large deflections. The definition of IDCS is not only beneficial for this work, but also it enables spatial CMs to be characterized, and the major effective design parameters of a spatial system to be identified. It can also be used to quantify the comparison of alternate solutions. The metric (DC) was defined as a quantitative measure for the change of stiffnesses in different configurations of an adaptive CM. Finally, experiments on prototypes were conducted to validate the simulation-based behavior.

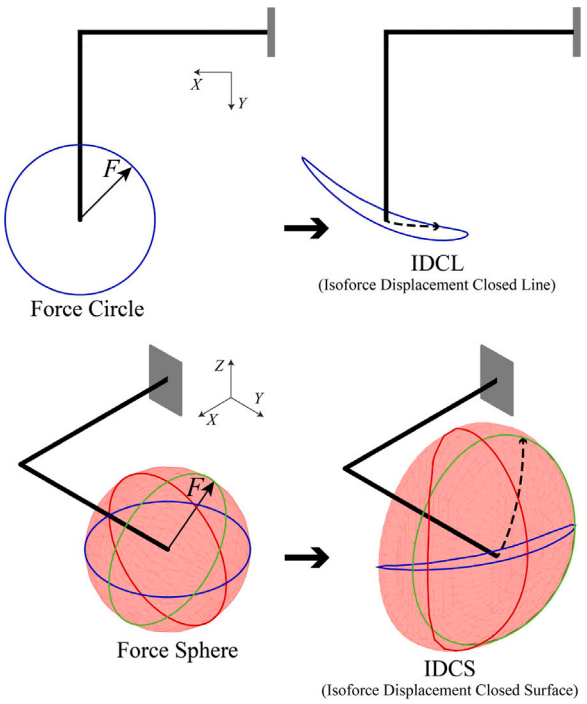

Fig. 1. The top figures show the forming process of an L-shaped cantilever beam's *Isoforce Displacement Closed Line* (IDCL) from a tip force circle in the XY plane. The bottom figures show the forming process of the same beam's *Isoforce Displacement Closed Surface* (IDCS) from a tip force sphere in 3D. Three IDCLs are shown as closed curves on the IDCS. These IDCLs result from the force circles of the same color in the XY, XZ, and YZ planes. A force vector $\vec{F}$ is shown in solid black and its curved representative displacement path as a result of gradually increasing force $\vec{F}$ is also shown with dashed black.

The paper is structured as follows. In Section 2, the concept for visualization of endpoint kinetostatic behavior is introduced. The definition of the problem and effective parameters together with the finite element solver are elaborated in Section 3. Additionally, the context of experimental verification procedures is discussed. In Section 4 the resulting behavior from different conditions is shown. A discussion on the validity of the results and possible other applications and future improvements are given in Section 5, and the conclusion is given in Section 6.

2. Preliminaries

In this section, we present a concept for the visualization of the nonlinear kinetostatic behavior of a CM for large deflections by introducing *Isoforce Displacement Closed Line* (IDCL), and *Isoforce Displacement Closed Surface* (IDCS). An IDCL is obtained by loading a point of interest, typically the endpoint, of a CM by a force circle (see Fig. 1), meaning that a force ($\vec{F}$) of a constant magnitude is applied in a 360° sweep, and interconnecting all of the endpoint's displaced positions makes the IDCL. We have introduced this closed curve shape previously in [51].

With the same logic, an IDCS is the interconnection of all of the point of interest's deflected positions when it is loaded by a force sphere. It is worth noting that, an IDCL is a closed curve on the IDCS surface. Fig. 1 shows the IDCS and three IDCLs of an "L" shaped beam with a circular cross section. The IDCLs are the results of force circles on the XY, XZ, and YZ planes.

As is suggested in Fig. 1, the nonlinear displacement as a result of a force vector in a specific direction is not by definition in the direction of the force itself. Therefore, it is not valid to assume each point of IDCL

and IDCS as a direct representation of the endpoint compliance in that direction. However, these graphical characterizations can clearly show the nonlinear kinetostatic behavior of a point of interest on a CM.

A similar concept for the characterization of the kinetostatic behavior of compliant building blocks was previously introduced by Kim et al. [52] as "compliance ellipsoids". The presented method in that work is analytical and easier to derive for simpler typologies, however, it only illustrates three main compliance vectors of a point of interest of a mechanism in each instance. Additionally, it only indicates the linear tangent stiffness. Thus, it is mainly effective for small deflections and it is not dependent on the magnitude of the force. In contrast, by employing IDCS, nonlinearities can be demonstrated; as a consequence, a change in force magnitude may result in a different IDCS.

In this study, the proposed graphical characterization method is used to demonstrate the spatial kinetostatic behavior of the beams' endpoints, as well as to elucidate variations in this behavior caused by different bellow configurations. This method of visualization can clarify the influence of torsional stiffening in the suggested combined design of the existing compliant mechanism. Noting that, as stated, we are proposing a method for changing stiffness and are not interested in a particular application for this method, it is essential to demonstrate changes in overall behavior that are not dependent on a particular application or direction; therefore, proposing this visualization is more important.

3. Methods

A slender cruciform clamped-free beam with a predetermined shape was used as the main compliant part, and a shorter bellow was employed as the torsional stiffener, as shown in Fig. 2(a). The bellow was sixty times stiffer in torsion than the beam, and its bending stiffness was approximately one-tenth of the beam bending stiffness. The bellow is only connected to the main beam with its side clamps. We hypothesized that altering the configuration of the bellows would result in significant changes in endpoint stiffness. To aid in the investigation of this mechanical behavior, various steps are detailed in this section.

The mechanism's topology and detailed parameters of the cruciform beam and bellow are discussed in the first step. The defined graphical characterization method for facilitating comprehension of changes in the beam's endpoint behavior in various bellow configurations is then elaborated. The details of implementing a geometrically nonlinear finite element beam model are discussed. Finally, the details of experimental beam prototyping and the test setup for verifying simulated results are elaborated.

3.1. Definition of topology

The cruciform beam was designed to be in a 1 m cube design space and have a spatial form. To make the shape of the beam extreme, the beam is set to move along all three principal axes. Therefore, the beam shape was formed in a way to travel the internal diagonal of a 1 m cube via its edges. However, following the cube corners could lead to sharp changes in the beam shape, which might lead to discontinuities in the finite element model, also stopping prismatic movement of the bellow along the beam. Therefore, to have a smooth shape for the beam, it was chosen to be formed based on a degree-two B-spline in which four corners of a 1 m cube were used as control points. The B-spline was chosen to have an open uniform knot vector of $[0, 0, 0, 0.5, 1, 1, 1]$. The position of the grounding point was assumed to be at the origin of the Cartesian coordinate system, and the beam endpoint was located at $[1, 1, 1]$. There were six different possibilities for the beam shape. The resultant shapes are shown in Fig. 3. A guide curve was determined to define the orientation of the cross-section in each point. Each beam section was set to be normal to the B-spline and the upper flange of the cruciform was designed to always point to the guide curve, which is shown in Fig. 3 with a red line. By defining this shape, we ensure

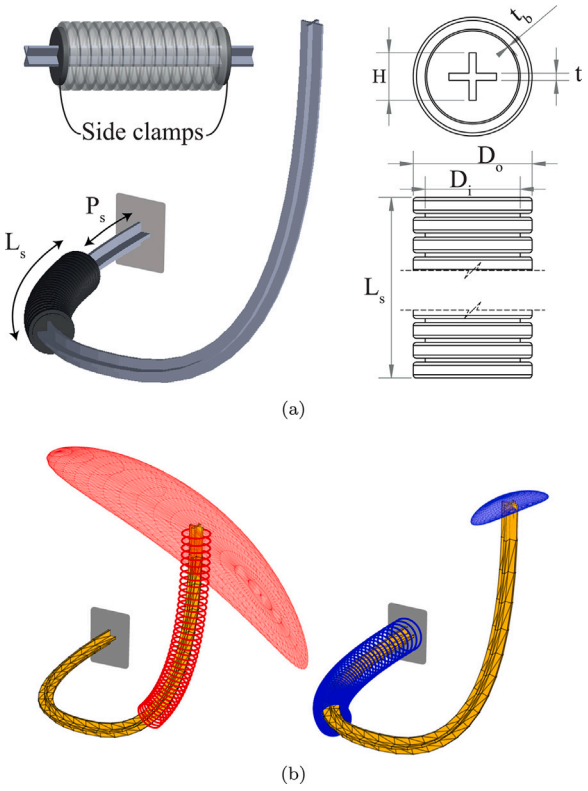

Fig. 2. (a) The cantilever cruciform beam and its movable torsional stiffener. The length of the sliding bellow is defined as L_s and its starting position on the beam named as P_s. The bellow is only connected to the beam with two thin clamps on the sides. (b) The Isoforce Displacement Closed Surface (IDCS) of the mechanism endpoint in two configurations of the bellow stiffener (red and blue).

that the beam is smooth enough for the bellow movement, and that it has parts oriented in the main Cartesian directions.

In the end, we selected only one beam out of all six possibilities, because the aim here was to capture the endpoint spatial behavior in different configurations of stiffener. After preliminary simulations, we discovered that the endpoint behavior of all six beam shapes follows the same pattern, meaning that all six beams show the same IDCS shape in a rotated or mirrored situation. Hence, we continued with only one beam out of six. The selected beam is shown in solid yellow in Fig. 3.

The bellow and cruciform cross-sectional dimensions, where the bellow length L_s was defined as a fraction of the main beam length L_b, are shown in Fig. 2(a). This figure also shows how the bellow was assembled on the beam by partially covering it. The bellow and beam connections, i.e. the side clamps in Fig. 2(a) were only on the sides of the bellow, where two circular parts with 2 mm thickness and a cruciform section cut were connected to the bellow sides. The bellow starting position from the beam base was labeled as P_s and it can slide on the beam. The value of P_s was expressed as a fraction of the main beam length and cannot be greater than $1-L_s$ in order to accommodate the bellow on the beam. Fig. 2(b) depicts two different positions of a bellow (red and blue) and the resulting IDCSs.

3.2. Cruciform beam and bellow stiffener dimensions

As shown in Fig. 2(a), the dimensions of the cruciform section were $H = W = 0.06$ m in height and width and $t = 0.009$ m in thickness.

For the bellow there were two diameters $D_{out} = 0.15$ m, $D_{in} = 0.12$ m and a uniform thickness $t_b = 0.0018$ m.

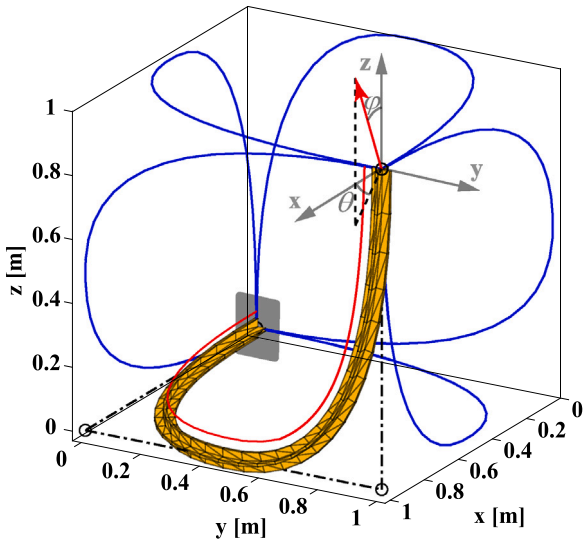

Fig. 3. All possible shapes for the spatial cantilever beam traveling from $[0,0,0]$ to $[1,1,1]$ according to the defined B-spline and control points on the edges of a virtual 1*1*1 cube are shown with blue lines. The selected beam's shape from six possible shapes and its control points are demonstrated. The guide curve specifying cross-sectional orientation is shown with the red line. Also, a local spherical coordinate system is set up at the end of the beam to make it easier to show the direction of the tip force.

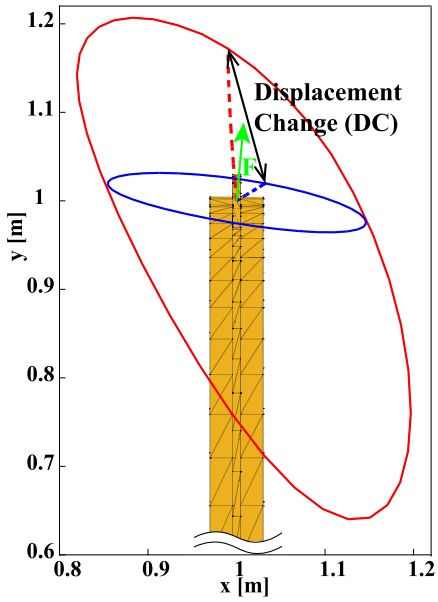

Fig. 4. The figure shows two Isoforce Displacement Closed Lines (IDCLs) for two bellow configurations (red and blue lines), and the displacement paths as a result of gradually increasing force $\vec{F}$ for each bellow configuration with dashed red and blue. Displacement Change (DC) is the magnitude of the difference between these two displacement vectors.

3.3. Isoforce Displacement Closed Surface (IDCS)

It is essential to have an understanding of the endpoint spatial kinetostatic behavior to realize changes determined by different bellow configurations. For this reason, we used IDCS for different bellow positions and lengths. To implement the tip force sphere, a spherical coordinate system was defined on the endpoint, as shown in Fig. 3. The in-plane angle θ of $\vec{F}$ was changed in 10° steps from 0° to 350° to form IDCLs. This procedure was repeated in planes with 36 different φ from 0° to 175° to make an IDCS from 36*36 displaced states for each bellow configuration. The resulted IDCS of these points are shown in Fig. 7. The magnitude of force was chosen to be three Newton ($\|\vec{F}\| = 3\,\mathrm{N}$), this led to the maximum equivalent (von Mises) stress of 32.8 MPa, which is below 68% of the yield stress (48 MPa) of the prototype material (PA-12). This force magnitude can be different for other materials and possibly lead to a bigger or smaller volume of IDCS.

3.4. Displacement Change (DC)

To have a clear quantified estimation of changes in the endpoint's stiffness, a metric was defined as *Displacement Change* (DC). This value was defined as the absolute magnitude of the displacement difference between two bellow configurations as a result of the same force vector ($\vec{F}$). To make this number dimensionless, we divided it by the base beam length (L_b). The formulation for so-called DC is:

$$DC = \frac{\left\| \vec{d}_{\,i}(\theta,\varphi) - \vec{d}_{\,e}(\theta,\varphi) \right\|}{L_b} \tag{1}$$

where d_i and d_e are displacement vectors as a result of the initial and the end configurations of the bellow, and φ, θ are respectively polar and azimuthal angle of the exerted tip force (see Fig. 4).

Finding the directions of the maximum and the minimum DC could be an intriguing aspect of the kinetostatic change. For this reason, a search function was used to find the force direction (θ,φ) among all 36*36 deformed states, which led to the Highest Displacement Change (HDC) and the Lowest Displacement Change (LDC).

To find DC, we always compared two different positions of the same bellow. As the bellows had the lowest effect when they were placed at the top end of the beam, we always calculated HDC and LDC between the highest possible position of the bellows (P_{s_e}) as the benchmark and other positions (P_{s_i}). It is important to mention that the bellow was designed to always remain on the beam, hence, P_{s_i} could only range from 0 to $1-L_s$ while P_{s_e} (benchmark configuration) was always equal to $1-L_s$.

The HDC direction can be interpreted as the direction where the endpoint behavior is affected most by changes in bellow position, and with the same logic, the LDC direction is the direction where changes in bellow have the least kinetostatic effect.

3.5. Finite element modeling

To simplify the model in finite element analysis, the parts of the beam covered by the torsional stiffener have been replaced by elements with the combined stiffness of the beam and stiffener. To obtain the IDCS, we needed to find the combined beam's endpoint displacements under 36*36 different loading vectors, and do this for each bellow configuration. Also, most of these loadings lead to large deformations. Hence, a relatively fast self-developed beam model was implemented. The solver uses geometrically nonlinear co-rotational beam elements, which were introduced by Battini [53], this model has been further explained in detail in [51].

A mesh converged solution with 30 elements for the beam length was used. As it mentioned the bellow stiffening effect were modeled by multiplying the I_{yy}, I_{zz} of bellow covered elements by 1.13 and their J by 60.8 regarding the data in Table 1. For different lengths of the bellows the number of covered elements was changed. 15, 10 and 5 elements respectively for long, medium, and short bellows, and for different heights of the bellow on the beam, the starting stiffened element was changed.

It is important to note that, we are employing the described finite element model as a tool in our work, as it is a well-established gold standard model and performs sufficiently for this application. It is clear

Table 1
The parameters for the bellow and the beam.

	Beam	Bellow
Area (m^2)	9.99e−4	4.48e−4
I_{yy} (m^4)	1.65e−7	2.23e−8
I_{zz} (m^4)	1.65e−7	2.23e−8
J (m^4)	2.64e−8	1.56e−6

Fig. 5. The experimental setup with a suspended-weight represents the constant magnitude of the tip force and a universal joint at clamping to represent the changes in load direction. The spatial displacement of the endpoint was measured using image processing of unloaded and loaded states from two perpendicular angles.

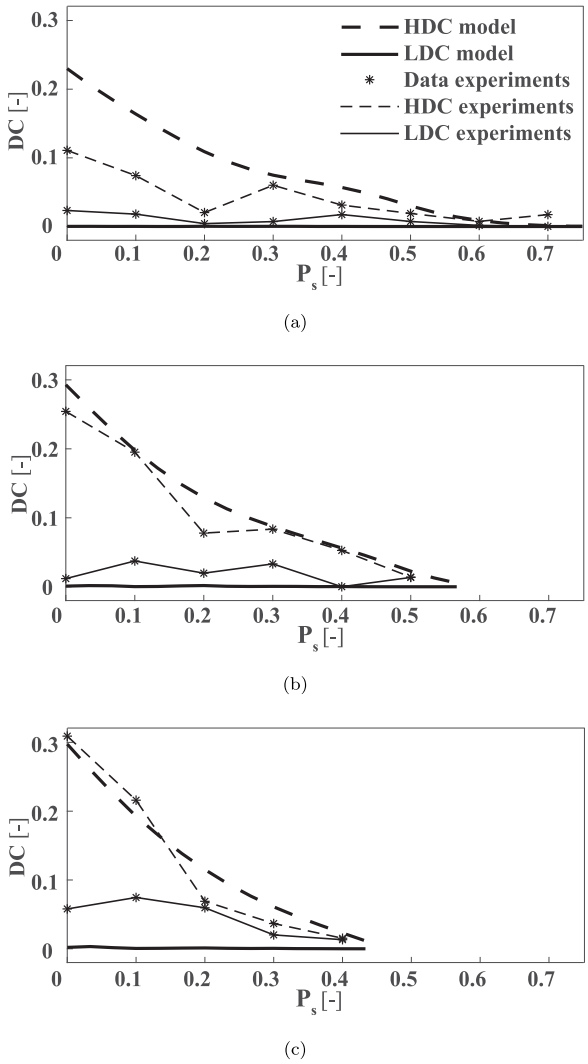

Fig. 6. Displacement Change (DC) as a result of the same magnitude of force in the Lowest DC (LDC, solid lines) and the Highest DC (HDC, dashed lines) directions upon different bellow positions (P_s). Figures (a), (b), (c) are respectively for short, medium, and long bellows.

that alternative more advanced models can also be used with the same visualization and layout as those described in this study.

Both the bellow and the cruciform beam were modeled as 3D Euler–Bernoulli beam. Therefore, all dimensions were ultimately reduced into four main beam parameters: area, second moment of inertia in the two main directions, and torsional constant. Based on the dimensions and the preliminary experiments, the parameters for modeling these two components are mentioned in Table 1.

For finding the Young's modulus (E), we conducted preliminary experiments on the bellow and beam prototypes. These tests resulted in $E = 1.17$ GPa. By using the Poisson's ratio of PA-12 [54], the shear modulus was calculated as $G = 0.41$ GPa for both the beam and the bellow.

3.6. Experiments

To validate modeling results, an experimental setup was developed. The prototypes for the experiments were 3D-printed using the multi-jet fusion method with PA-12 as the material. The beams were down-scaled six times to fit within the printing volume.

The experiments included loading the endpoint in LDC and HDC directions obtained from simulations (see Table 2), with $\overline{F} = 3\,\mathrm{N}/scale = 0.5\,\mathrm{N}$, and capturing the undeformed and deformed states to find the experimental HDC and LDC (see Fig. 6).

Here, we used suspended weight as the load. This load was always pointing vertically downward. Therefore, to implement the load's different directions, the whole mechanism was clamped onto a universal rotational stage where the rotation of the beam's global coordinates in θ and φ represented the changes in endpoint load direction. The experimental setup is shown in Fig. 5.

The three-dimensional displacement in the loaded and unloaded states were obtained by tracking the displacement of the endpoint marker in images that were taken from two perpendicularly located cameras.

4. Results

To understand the effect of torsional stiffener length, three different bellows were chosen with their length (L_s) indicated as a fraction of the main beam length (L_b). The bellow lengths were selected to be 1/2 (long), 1/3 (medium), and 1/6 (short) of L_b. Besides the length of the bellow, the effect of its starting position (P_s) was also investigated.

The resultant HDC and LDC of these different positions are shown in Fig. 6 with thick dashed lines for HDC and thick solid lines for LDC. The directions of the forces for LDC and HDC in different configurations

Table 2
The directions of the force to obtain the Lowest Displacement Change (LDC) and the Highest Displacement Change (HDC) in different positions of the bellow ($P_s = 0 - 0.7$). θ and φ are resulted from modeling and used for the experiments. The resulted HDC, LDC, and HDC/LDC from experiments are also shown for all bellow lengths (long, medium and, short).

P_s (position)	Long							Medium							Short						
	LDC			HDC			HDC/LDC	LDC			HDC			HDC/LDC	LDC			HDC			HDC/LDC
	Direction		LDCe-2	Direction		HDCe-2		Direction		LDCe-2	Direction		HDCe-2		Direction		LDCe-2	Direction		HDCe-2	
	θ	φ		θ	φ			θ	φ		θ	φ			θ	φ		θ	φ		
0	40	50	5.8	110	150	**30.9**	5.3	50	45	1.2	120	160	**25.4**	21.5	50	40	2.3	90	160	**11.1**	4.7
0.1	70	30	7.5	130	155	**21.6**	2.9	70	30	3.7	150	160	**19.5**	5.2	50	40	1.8	130	165	**7.4**	4.1
0.2	70	30	6.0	150	160	**6.9**	1.2	90	20	2.0	160	145	**7.8**	3.9	70	30	0.3	150	160	**2.0**	7.5
0.3	90	20	2.0	160	145	**3.7**	1.8	90	20	3.3	170	130	**8.4**	2.5	90	20	0.7	180	140	**6.0**	8.3
0.4	80	30	1.3	170	130	**1.5**	1.2	90	20	0.9	180	115	**5.3**	6.1	90	10	1.7	180	120	**3.1**	1.8
0.5								280	30	1.4	180	110	**1.4**	1	90	20	0.7	180	110	**1.9**	2.6
0.6															280	30	0.2	180	115	**0.7**	4.7
0.7															280	30	0.2	180	120	**1.7**	8.5

Table 3
The Normalized Root Mean Square Error (NRMSE) for different sets of experimental results compared to finite element results. The errors for long, medium, and short bellows, in the Lowest Displacement Change (LDC) and the Highest Displacement Change (HDC) are shown.

	Long		Medium		Short	
	LDC	HDC	LDC	HDC	LDC	HDC
NRMSE	16.2%	8.2%	8.6%	7.7%	5.5%	27.9%

are shown in Table 2. It is clear that with a longer bellow, the range of motion for the bellow becomes shorter. Hence, in Fig. 6 the horizontal axis (P_s) for longer bellow is shorter.

In addition, for each of the three bellow lengths in Fig. 7 (a, c, e), we have also shown the IDCS of the two most extreme positions ($P_s = 1 - L_s, 0$). In the same figure, the displacement path of the beam in two configurations with HDC (dashed lines) and LDC (solid lines) are also shown (b,d,f). The blue and red lines and surfaces are for the blue and red configurations of the bellows.

4.1. Experimental results

Experiments were used to determine the displacements of the mechanism with various bellow configurations. The mechanism displacements were found in discrete positions and normalized based on the length of the prototype beam to be comparable with modeling results. The resultant DCs from experiments are shown with an asterisk (*) in Fig. 6. To make the experimental results trend comparable with the simulation results, the data points are connected with the thin dashed (HDC) and thin solid (LDC) lines.

A Normalized Root Mean Square Error (NRMSE) is used for each set of experimental results to show the difference with finite element results. For normalization of the RMSE, each set of results is divided by its *"max value - min value"*. Table 3 shows the NRMSE for different sets.

5. Discussion

The results highlighted the effect of torsional stiffening on the endpoint behavior of the CM and the anisotropically adaptive stiffness that was achieved with this technique. It was shown that meaningful trends in the nonlinear kinetostatic behavior of the mechanism can be achieved by changing configurations of the bellow. These changes are further analyzed by the graphical characterization method and the metric, IDCSs and HDC, which were specifically defined to understand the behavior of spatial CM.

In Fig. 7, the difference between the IDCSs of the two configurations of the bellow, blue and red, becomes more significant as the length of the bellow increases. Also, from Fig. 6 it can be revealed that with longer bellows, we can achieve higher HDC. However, a shorter bellow has a greater travel range than a longer bellow, and it is more appropriate for having a fine control on the endpoint behavior. Hence, there is a trade off between having a higher stiffness change (longer bellow) or a wider range of adjustment (shorter bellow) when choosing the bellow length.

Fig. 6 also shows that the effect of the change in bellow position is higher near the grounding of the beam. This nonlinear decrease in HDC is due to the fact that with the current topology of the clamped-free beam, the base elements are subjected to higher deformation due to larger moment arms, and their deformations have a larger effect on the endpoint displacement.

As anticipated, both Figs. 6 and 7 confirm that the changes in endpoint behavior are not isotropic. The reason behind this behavior can be explained by an example. If we imagine a tip force in the Y direction in Fig. 3 on the beam, it will cause bending of the Z and Y-oriented parts of the beam and torsion of the X-oriented part. Regarding the fact that the deformation of the endpoint is heavily dependent on the beam base and that the moments are higher in the base part. Therefore, the torsion in the X-oriented part of the beam plays the major role. Hence, by torsionally stiffening this part, we can expect higher overall stiffness of the endpoint in the Y direction.

If we imagine the same situation for a tip force in the X direction, it will cause bending in the Z-oriented and X-oriented parts of the beam and torsion in the Y-oriented part. However, we mentioned that the effect of the beam base (the X-oriented part) is much more important. Therefore, torsional stiffening of the beam base will not cause a significant change in stiffness for the endpoint in the X direction.

Regarding this explanation, we can state that, by torsional stiffening of the beam, the endpoint stiffness behavior changes significantly in the directions wherein the torsion of the base elements is dominant, namely the Y direction in Fig. 3 which causes the HDC direction, and it almost remains the same in directions where the bending of the base part is dominating, namely the X direction, which causes the LDC direction.

In Fig. 6, the solid LDC lines are representative of bending-dominated directions, where the overall stiffness of the structure remains almost the same, and therefore, the DC remains almost zero regardless of the length and position of the bellow. With the same logic, the dashed HDC lines are representative of torsion-dominated directions where the endpoint stiffness is affected significantly by the torsional stiffening caused by the bellow.

The experimental results arguably match the anticipated results from finite element modeling, and the highest achievable HDCs in two cases are comparable. The reason behind some mismatches can be found in different assumptions:

Firstly, in the finite element modeling, we assumed that the stiffened beam parts, i.e. beam parts that are covered by the bellow, can be replaced by beam elements with the combined stiffness of the beam and bellow, whereas in reality, the bellow is only connected to the beam on two side clamps. The modeling of this stiffening could be captured better by taking the bellow and beam as parallel elements between

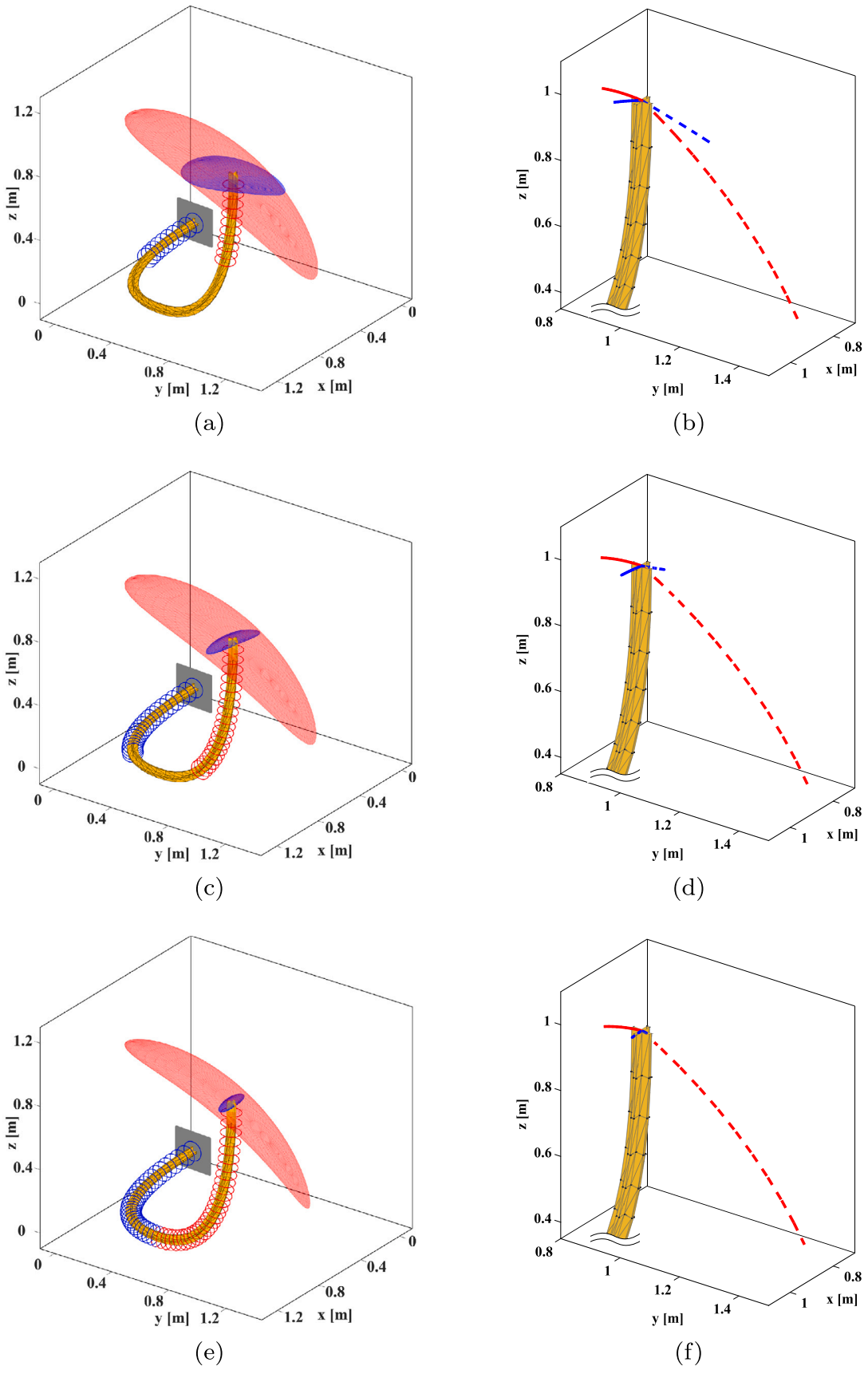

Fig. 7. The left figures show the resulting Isoforce Displacement Closed Surfaces (IDCSs) for two positions of the bellow, on top and bottom of the beam. Blue IDCS is for the bottom blue position, and red IDCS is for the top red position of the bellow. The right figures show the displacement path of the endpoint for the same two positions of the bellow on the top and bottom, where the blue lines are for the bottom position and the red lines are for the top position of the bellow. The displacement paths are shown for two different directions of the load in each of the two bellow position, HDC load direction (dashed lines) and LDC load direction (solid lines). The displacement paths are the result of gradually increasing loads in that direction. Figures (a, b), (c, d), (e, f) are respectively for short, medium, and long bellows.

clamping points and constraining them only on the side clamps of the bellow.

Secondly, here we have used Bernoulli's beam model, which is a gold standard for this type of structure, but it cannot capture some forms of deformation, e.g., section deformation. Using a more advanced finite element model can lead to a lower mismatch between experiments and modeling. Furthermore, in the current model, increasing the number of simulations per each configuration of the bellow can improve the resolution of θ and φ for HDC and LDC directions.

Thirdly, there were sources of error in the measurement setup, e.g., the torsion of the beam curve and the bellow were not matched in all configurations. Moreover, with the current bellow-beam connection, there is still room for under-bending of the bellow and over-torsion of the covered part of the beam, which makes the model less valid and shows its effect mainly on the most extreme cases, i.e., LDC of the long bellow and HDC of the short bellow (Fig. 6(a) dashed line and Fig. 6(c) solid line).

Another source of error can be considered in the bending stiffness of the bellow, which was assumed to be linear. However, initial investigations have shown that in large deformations, the bellow exhibits bending stiffening and it shows nonlinear behavior.

Eliminating these major causes of errors can result in a better match between modeling and experiments. However, the current data already demonstrate the desired behavior, and the conclusion regarding the change of kinetostatic behavior remains sound.

Attention must be paid to the definition of what we are achieving in terms of changes in endpoint kinetostatic behavior as the displacement vectors are not in the same direction as the forces due to the coupled parameters in the endpoint stiffness matrix (see Fig. 1). Also, in most cases, as it is shown in Fig. 7(b,d,f), we observed a curved path and nonlinear deformation of the endpoint due to the large magnitude of the force. Hence, the arbitrarily selected magnitude of the endpoint force has an effect on the maximum achievable HDC/LDC, but the overall anisotropic adaptive stiffness behavior due to torsional stiffening of the spatial mechanism is present regardless of the force amplitude.

Here, torsional stiffening was selected as the primary way to achieve anisotropically variable behavior. It is possible to achieve this behavior for other types of spatial structures as well, e.g., thin-walled shells. Also, changing the torsional stiffness is possible with other methods.

The resulting anisotropic change in the displacement domain is an interesting effect that can be used in many ways, such as in exoskeletons or morphing wings, where the stiffness needs to be reduced in one direction but stay more or less the same in other directions.

The optimization of several arbitrarily selected parameters like the shape and cross section of the beam and its torsion to bending stiffness ratio can notably change the behavior of the mechanism and further enhance the DC and anisotropy of the system. Hence, it is possible to use this simple, effective technique to design and modify the endpoint characterization of other spatial compliant systems, specifically for applications where weight and slenderness are key requirements.

6. Conclusion

We have presented a method which allows for anisotropic changes of end point stiffness of a spatial CM. This is done by a novel combination of two contrasting parts: a clamped-free curved cruciform beam with relatively high bending and low torsional stiffness as the base structure, and a short bellow with low bending and high torsional stiffness as a prismatic torsional stiffener of the main beam.

A graphical characterization method has been introduced to investigate the three dimensional nonlinear changes of the mechanism's endpoint's behavior due to the variation of the length and position of the bellow. This visualization can further be used to characterize the kinetostatic behavior of other types of spatial CM.

21.5 times higher stiffness changes in one direction compared to the other was achieved in the experiments using this method. The simulated behavior was also verified by observing similar trend of changes with experiments with an averaged normalized RMS error of 12.5%.

This type of anisotropic adaptive stiffness can have several applications where changes only in one direction's stiffness are required while the other direction's stiffness should remain almost the same. A similar combination of contrasting elements can be used for other types of structures like thin-walled shells. It is also possible to implement optimization on effective parameters of the current design to further enhance the presented feature.

CRediT authorship contribution statement

Ali Amoozandeh Nobaveh: Conceptualization, Methodology, Software, Validation, Formal analysis, Investigation, Writing – original draft. **Giuseppe Radaelli:** Conceptualization, Methodology, Software, Writing – review & editing, Supervision, Project administration. **Werner W.P.J. van de Sande:** Software, Writing – review & editing. **Ron A.J. van Ostayen:** Conceptualization, Writing – review & editing, Supervision. **Just L. Herder:** Conceptualization, Writing – review & editing, Supervision, Project administration, Funding acquisition.

Declaration of competing interest

The authors declare that they have no known competing financial interests or personal relationships that could have appeared to influence the work reported in this paper.

Data availability

Data will be made available on request.

Acknowledgment

This work was supported by the Dutch Research Council (NWO), Netherlands [P16-05 Shell-Skeletons].

References

[1] Barbarino S, Bilgen O, Ajaj RM, Friswell MI, Inman DJ. A review of morphing aircraft. J Intell Mater Syst Struct 2011;22(9):823–77.
[2] Thuwis GA, Abdalla MM, Gürdal Z. Optimization of a variable-stiffness skin for morphing high-lift devices. Smart Mater Struct 2010;19(12):124010.
[3] Chen Z, Wu X, Wang Z, Shao J. Concepts for morphing airfoil using novel auxetic lattices. In: International conference on aerospace system science and engineering. Springer; 2019, p. 265–74.
[4] Nicassio F, Scarselli G, Pinto F, Ciampa F, Iervolino O, Meo M. Low energy actuation technique of bistable composites for aircraft morphing. Aerosp Sci Technol 2018;75:35–46.
[5] Kuder IK, Arrieta AF, Raither WE, Ermanni P. Variable stiffness material and structural concepts for morphing applications. Prog Aerosp Sci 2013;63:33–55.
[6] Sun J, Guan Q, Liu Y, Leng J. Morphing aircraft based on smart materials and structures: A state-of-the-art review. J Intell Mater Syst Struct 2016;27(17):2289–312.
[7] Manti M, Cacucciolo V, Cianchetti M. Stiffening in soft robotics: A review of the state of the art. IEEE Robot Autom Mag 2016;23(3):93–106.
[8] Fang B, Sun F, Wu L, Liu F, Wang X, Huang H, et al. Multimode grasping soft gripper achieved by layer jamming structure and tendon-driven mechanism. Soft Robotics 2022;9(2):233–49.
[9] Crowley GB, Zeng X, Su H-J. A 3D printed soft robotic gripper with a variable stiffness enabled by a novel positive pressure layer jamming technology. IEEE Robot Autom Lett 2022;7(2):5477–82.
[10] Arachchige DD, Chen Y, Walker ID, Godage IS. A novel variable stiffness soft robotic gripper. In: 2021 IEEE 17th international conference on automation science and engineering. IEEE; 2021, p. 2222–7.
[11] Wall V, Deimel R, Brock O. Selective stiffening of soft actuators based on jamming. In: 2015 IEEE international conference on robotics and automation. IEEE; 2015, p. 252–7.
[12] Al Abeach L, Nefti-Meziani S, Theodoridis T, Davis S, et al. A variable stiffness soft gripper using granular jamming and biologically inspired pneumatic muscles. J Bionic Eng 2018;15(2):236–46.

[13] Hauser S, Robertson M, Ijspeert A, Paik J. Jammjoint: A variable stiffness device based on granular jamming for wearable joint support. IEEE Robot Autom Lett 2017;2(2):849–55.
[14] Gao Y, Huang X, Mann IS, Su H-J. A novel variable stiffness compliant robotic gripper based on layer jamming. J Mech Robot 2020;12(5):051013.
[15] Zhu M, Mori Y, Wakayama T, Wada A, Kawamura S. A fully multi-material three-dimensional printed soft gripper with variable stiffness for robust grasping. Soft Robotics 2019;6(4):507–19.
[16] Gerez L, Gao G, Liarokapis M. Laminar jamming flexure joints for the development of variable stiffness robot grippers and hands. In: 2020 IEEE/RSJ international conference on intelligent robots and systems. IEEE; 2020, p. 8709–15.
[17] Yang Y, Zhang Y, Kan Z, Zeng J, Wang MY. Hybrid jamming for bioinspired soft robotic fingers. Soft Robotics 2020;7(3):292–308.
[18] Kim Y-J, Cheng S, Kim S, Iagnemma K. A stiffness-adjustable hyperredundant manipulator using a variable neutral-line mechanism for minimally invasive surgery. IEEE Trans Robot 2013;30(2):382–95.
[19] De Falco I, Cianchetti M, Menciassi A. A soft multi-module manipulator with variable stiffness for minimally invasive surgery. Bioinspiration Biomim 2017;12(5):056008.
[20] Jiang A, Xynogalas G, Dasgupta P, Althoefer K, Nanayakkara T. Design of a variable stiffness flexible manipulator with composite granular jamming and membrane coupling. In: 2012 IEEE/RSJ international conference on intelligent robots and systems. IEEE; 2012, p. 2922–7.
[21] Blanc L, Delchambre A, Lambert P. Flexible medical devices: Review of controllable stiffness solutions. Actuators 2017;6(3):23.
[22] Baniasadi M, Foyouzat A, Baghani M. Multiple shape memory effect for smart helical springs with variable stiffness over time and temperature. Int J Mech Sci 2020;182:105742.
[23] Adeodato A, Duarte BT, Monteiro LLS, Pacheco PMC, Savi MA. Synergistic use of piezoelectric and shape memory alloy elements for vibration-based energy harvesting. Int J Mech Sci 2021;194:106206.
[24] Radaelli G, Rosenberg EJ, Aguirre ME, Verkuyl AC, Wisse BM. Wearable support structure and method of supporting a torso. 2020, Google Patents, US Patent 10, 561, 518.
[25] Dunning A, Stroo J, Radaelli G, Herder J. Feasibility study of an upper arm support based on bending beams. In: 2015 IEEE international conference on rehabilitation robotics. IEEE; 2015, p. 520–5.
[26] del Carmen Sanchez-Villamañan M, Gonzalez-Vargas J, Torricelli D, Moreno JC, Pons JL. Compliant lower limb exoskeletons: a comprehensive review on mechanical design principles. J Neuroeng Rehabil 2019;16(1):55.
[27] Yuan S, Sun Y, Wang M, Ding J, Zhao J, Huang Y, et al. Tunable negative stiffness spring using maxwell normal stress. Int J Mech Sci 2021;193:106127.
[28] Doumit M, Leclair J. Development and testing of stiffness model for pneumatic artificial muscle. Int J Mech Sci 2017;120:30–41.
[29] Akhavan H, Ribeiro P, De Moura M. Large deflection and stresses in variable stiffness composite laminates with curvilinear fibres. Int J Mech Sci 2013;73:14–26.
[30] Jin T, Liu Z, Sun S, Ren Z, Deng L, Ning D, et al. Theoretical and experimental investigation of a stiffness-controllable suspension for railway vehicles to avoid resonance. Int J Mech Sci 2020;187:105901.
[31] Lachenal X, Daynes S, Weaver PM. A zero torsional stiffness twist morphing blade as a wind turbine load alleviation device. Smart Mater Struct 2013;22(6):065016.
[32] Lachenal X, Daynes S, Weaver PM. Review of morphing concepts and materials for wind turbine blade applications. Wind Energy 2013;16(2):283–307.
[33] del Carmen Sanchez-Villamañan M, Gonzalez-Vargas J, Torricelli D, Moreno JC, Pons JL. Compliant lower limb exoskeletons: a comprehensive review on mechanical design principles. J Neuroeng Rehabil 2019;16(1):1–16.
[34] Amoozandeh Nobaveh A, Radaelli G, Herder JL. A design tool for passive wrist support. In: International Symposium on Wearable Robotics. Springer; 2020, p. 13 – 17.
[35] Lin L, Zhang F, Yang L, Fu Y. Design and modeling of a hybrid soft-rigid hand exoskeleton for poststroke rehabilitation. Int J Mech Sci 2021;212:106831.
[36] Hull J, Turner R, Asbeck AT. Design and preliminary evaluation of two tool support arm exoskeletons with gravity compensation. Mech Mach Theory 2022;172:104802.
[37] Buccelli S, Tessari F, Fanin F, De Guglielmo L, Capitta G, Piezzo C, et al. A gravity-compensated upper-limb exoskeleton for functional rehabilitation of the shoulder complex. Appl Sci 2022;12(7):3364.
[38] Radaelli G. Synthesis of mechanisms with prescribed elastic load-displacement characteristics (Ph.D. thesis), Delft University of Technology, Delft, The Netherlands; 2017.
[39] Radaelli G, Herder J. Gravity balanced compliant shell mechanisms. Int J Solids Struct 2017;118:78–88.
[40] Tschiersky M, Hekman EE, Herder JL, Brouwer DM. Gravity balancing flexure spring mechanisms for shoulder support in assistive orthoses. IEEE Trans Med Robot Bionics 2022;4(2):448–59.
[41] Kok S, Radaelli G, Nobaveh AA, Herder J. Neutrally stable transition of a curved-crease planar shell structure. Extrem Mech Lett 2021;49:101469.
[42] Bilancia P, Berselli G, Bruzzone L, Fanghella P. A CAD/CAE integration framework for analyzing and designing spatial compliant mechanisms via pseudo-rigid-body methods. Robot Comput-Integr Manuf 2019;56:287–302.
[43] Nijssen J, Radaelli G, Kim CJ, Herder JL. Overview and kinetostatic characterization of compliant shell mechanism building blocks. J Mech Robot 2020;12(6).
[44] Weeger O, Narayanan B, Dunn ML. Isogeometric shape optimization of nonlinear, curved 3D beams and beam structures. Comput Methods Appl Mech Engrg 2019;345:26–51.
[45] Tridech C, Maples HA, Robinson P, Bismarck A. High performance composites with active stiffness control. ACS Appl Mater Interfaces 2013;5(18):9111–9.
[46] Ou J, Yao L, Tauber D, Steimle J, Niiyama R, Ishii H. jamSheets: thin interfaces with tunable stiffness enabled by layer jamming. In: Proceedings of the 8th international conference on tangible, embedded and embodied interaction. 2014, p. 65–72.
[47] Wang T, Zhang J, Li Y, Hong J, Wang MY. Electrostatic layer jamming variable stiffness for soft robotics. IEEE/ASME Trans Mechatronics 2019;24(2):424–33.
[48] Rad FP, Berselli G, Vertechy R, Castelli VP. Compliance based characterization of spherical flexure hinges for spatial compliant mechanisms. In: Advances on theory and practice of robots and manipulators. Springer; 2014, p. 401–9.
[49] Raither W, Bergamini A, Ermanni P. Profile beams with adaptive bending–twist coupling by adjustable shear centre location. J Intell Mater Syst Struct 2013;24(3):334–46.
[50] Ajaj R, Friswell M, Dettmer W, Isikveren A, Allegri G. Conceptual modeling of an adaptive torsion wing structure. In: 52nd AIAA/ASME/ASCE/AHS/ASC structures, structural dynamics and materials conference 19th AIAA/ASME/AHS adaptive structures conference 13t. 2011, p. 1883.
[51] Nobaveh AA, Radaelli G, Herder JL. Asymmetric spatial beams with symmetric kinetostatic behaviour. In: Symposium on robot design, dynamics and control. Springer; 2020, p. 247–54.
[52] Kim CJ, Moon Y-M, Kota S. A building block approach to the conceptual synthesis of compliant mechanisms utilizing compliance and stiffness ellipsoids. 2008.
[53] Battini J-M. Co-rotational beam elements (Ph.D. thesis), (January). Royal Institute of Technology, Stockholm, Sweden; 2002.
[54] Faes M, Wang Y, Lava P, Moens D. Variability in the mechanical properties of laser sintered PA-12 components. In: Proceedings of the 26th annual international solid freeform fabrication symposium. Solid freeform fabrication symposium. 2015, p. 847–56.